IFCP Riemann solver: Application to tsunami modelling using GPUs

M.J. Castro & M. de la Asunción & J. Macías & C. Parés
Dpto. Análisis Matemático. Universidad de Málaga. Campus de Teatinos, s/n. 29071 Málaga (Spain)

E. D. Fernández-Nieto
E.T.S. Arquitectura. Universidad de Sevilla. Avda, Reina Mercedes, s/n. 41012 Sevilla (Spain)

J.M. González-Vida
E.T.S. Telecomunicación. Universidad de Málaga. Campus de Teatinos, s/n. 29071 Málaga (Spain)

T. Morales
Departamento de Matemáticas. Universidad de Córdoba. Campus de Rabanales. 14071 Córdoba (Spain)

ABSTRACT: In this work, we present a simplified two-layer model of Savage-Hutter type to simulate tsunamis generated by landslides (see (Fernández et al. 2008)). A layer composed of fluidized granular material is assumed to flow within an upper layer composed of an inviscid fluid (e.g. water). The sediment layer is modelled by a Savage-Hutter type model where buoyancy effects have been considered. The system is discretized using IFCP finite volume scheme. The first order IFCP scheme was introduced in (Fernández et al. 2011) and it is constructed by using a suitable decomposition of a Roe matrix by means of a parabolic viscosity matrix, that captures information of the intermediate fields (Intermediate Field Capturing Parabola). Its extension to high order and two-dimensional domains is straightforward. To conclude, some numerical examples are presented.

1 INTRODUCTION

Let us consider a simplified two-layer Savage-Hutter type system that can be use to model tsunamis generated by landslides. This model is a simplified version of the one introduced in (Fernández et al. 2008): a layer composed of fluidized granular material is assumed to flow within an upper layer composed of an inviscid fluid (e.g. water). The sediment layer is modelled by a Savage-Hutter type model where buoyancy effects have been considered:

$$\left\{\begin{array}{l} \dfrac{\partial h_1}{\partial t}+\dfrac{\partial q_1}{\partial x}=0, \\ \dfrac{\partial q_1}{\partial t}+\dfrac{\partial}{\partial x}\left(\dfrac{q_1^2}{h_1}+\dfrac{g}{2}h_1^2\right) = -gh_1\dfrac{\partial h_2}{\partial x}-gh_1\dfrac{db}{dx} \\ \qquad\qquad +\tau_i, \\ \dfrac{\partial h_2}{\partial t}+\dfrac{\partial q_2}{\partial x}=0, \\ \dfrac{\partial q_2}{\partial t}+\dfrac{\partial}{\partial x}\left(\dfrac{q_2^2}{h_2}+\dfrac{g}{2}h_2^2\right) = -rgh_2\dfrac{\partial h_1}{\partial x}-gh_2\dfrac{db}{dx} \\ \qquad\qquad -r\tau_i-\tau_b \end{array}\right. \tag{1}$$

In these equations, index 1 makes reference to the upper layer (water) and index 2 to the lower one (granular material). The coordinate x refers to the axis of the channel, t is time, and g is the acceleration due to gravity. $b(x)$ represents the bathymetry. Each layer is assumed to have a constant density, ρ_i, $i=1,2$ ($\rho_1<\rho_2$), and $r=\rho_1/\rho_2$. The unknowns $q_i(x,t)$ and $h_i(x,t)$ represent respectively the mass-flow and the thickness of the i-th layer. τ_i is the friction term between the two layers and here it is written as

$$\tau_i = c_i\frac{h_1h_2}{rh_1+h_2}|u_1-u_2|(u_2-u_1),$$

and τ_b denotes the Coulomb friction term. This term must be understood as:

$$\text{If } |\tau_b|\geq\sigma_c \quad\Rightarrow\quad \tau_b = g(1-r)h_2\frac{u_2}{|u_2|}\tan(\delta_0), \tag{2}$$

$$\text{If } |\tau_b|<\sigma_c \quad\Rightarrow\quad u_2=0. \tag{3}$$

where $\sigma_c=g(1-r)h_2\tan(\delta_0)$, being δ_0 the Coulomb friction angle.

Observe that the presence of the term $(1-r)$ in the definition of the Coulomb friction term is due to the buoyancy effects, that must be taken into account only in the case that the sediment layer is submerged in the fluid, otherwise this term must be replaced by 1.

Notice that system (1) can be written in the following form:

$$w_t + F(w)_x + B(w)\cdot w_x = S(w)b_x + \boldsymbol{\tau}, \quad (4)$$

where

$$w(x,t) = \begin{bmatrix} h_1(x,t) \\ q_1(x,t) \\ h_2(x,t) \\ q_2(x,t) \end{bmatrix}, \quad F(w) = \begin{bmatrix} q_1 \\ \frac{q_1^2}{h_1} + \frac{g}{2}h_1^2 \\ q_2 \\ \frac{q_2^2}{h_2} + \frac{g}{2}h_2^2 \end{bmatrix},$$

$$S(w) = \begin{bmatrix} 0 \\ -gh_1 \\ 0 \\ -gh_2 \end{bmatrix}, \; B(w) = \begin{bmatrix} 0 & 0 & 0 & 0 \\ 0 & 0 & gh_1 & 0 \\ 0 & 0 & 0 & 0 \\ grh_2 & 0 & 0 & 0 \end{bmatrix},$$

$$\boldsymbol{\tau} = [0,\, \tau_i,\, 0,\, -r\tau_i - \tau_b\,]^T.$$

The vector w takes values in the set:

$$\mathcal{O} = \{[h_1, q_1, h_2, q_2]^T \in \mathbb{R}^4, \quad h_1 \geq 0,\; h_2 \geq 0\},$$

as the thickness of the layers may vanish in practical applications when one or the two layers disappear in part of the domain. Let us also define the matrix $A(w)$ given by

$$A(w) = J(w) + B(w), \quad \text{being } J(w) = \frac{\partial F}{\partial w}(w).$$

The characteristic equation of $A(w)$ is:

$$\left(\lambda^2 - 2u_1\lambda + u_1^2 - gh_1\right)\left(\lambda^2 - 2u_2\lambda + u_2^2 - gh_2\right) = rg^2h_1h_2. \quad (5)$$

It is easy to check that the condition under which one of the eigenvalues vanishes is:

$$G^2 = F_1^2 + F_2^2 - (1-r)F_1^2F_2^2 = 1, \quad (6)$$

where G is the so-called *composite Froude number*, and F_i for $i = 1, 2$ are the internal Froude numbers ($F_i^2 = \frac{u_i^2}{g'h_i}$, where g' is the *reduced gravity*, $g' = (1-r)g$). When this condition is achieved at a section of coordinate x, the flow is said to be *critical* at this point and the section x is called a *control*. When $G^2 < 1$, the flow is *subcritical*. Finally, when $G^2 > 1$, the flow is *supercritical*.

Observe that, when $r = 0$, the eigenvalues are those corresponding to each layer separately. Therefore, when $r \cong 0$, the coupling terms do not affect the nature of the system in an essential manner. The eigenvalues of A can be classified in two external and two internal eigenvalues. The external eigenvalues, $\lambda_{ext}^{\pm}$, are related to the propagation speed of barotropic perturbations and the internal ones $\lambda_{int}^{\pm}$, to the propagation of baroclinic perturbations. First order approximation of the eigenvalues can be found in (Schijf & Schonfeld 1953).

In most applications to geophysical flows, one has $\lambda_{ext}^{-} < 0$ and $\lambda_{ext}^{+} > 0$. Moreover, the internal eigenvalues depend on the reduced gravity g'. As a consequence the absolute value of internal eigenvalues are usually smaller than those of external ones, that is

$$|\lambda_{int}^{\pm}| < |\lambda_{ext}^{-}|, \quad |\lambda_{int}^{\pm}| < |\lambda_{ext}^{+}|.$$

This fact implies that first order numerical schemes that only use information concerning the external eigenvalues are in general too diffusive when applied to the simulation of internal waves. On the other hand, methods that use explicitly the eigenstructure of A, as it is the case of Roe method, are computationally expensive, as it does not exist any easy explicit expression of the eigenvalues and eigenvectors of this system. IFCP scheme is a computationally fast and precise method that uses information concerning the internal eigenvalues. The definition of the method is based on a suitable decomposition of a Roe matrix (see (Toumi 1992)) by means of a parabolic viscosity matrix (see (Degond et al. 1999)) that captures intermediate field information.

2 NUMERICAL SCHEME

Here, only the description of the 1D first and high order IFCP scheme is considered. Its extension to two-dimensional problems is straightforward following the procedure described in (Castro et al. 2009) and (Gallardo et al. 2011).

Friction terms $\boldsymbol{\tau}$ will be discretized semi-implicitly as described in (Fernández et al. 2008), so they are neglected at this point.

Solutions of (4) may develop discontinuities and, due to the non-divergence form of the equations, the notion of weak solution in the sense of distributions cannot be used. The theory introduced by Dal Maso, LeFloch, and Murat (Dal Maso et al. 1995) is followed here to define weak solutions of (4). This theory allows to define the nonconservative products as a bounded measure provided a family of Lipschitz continuous paths $\Phi : [0,1] \times \Omega \times \Omega \to \Omega$ is prescribed, which must satisfy certain natural regularity condi-

tions. Here, the family of straight segments is considered:

$$\Phi(s; w_L, w_R) = w_L + s(w_R - w_L).$$

In (Fernández et al. 2011) authors introduce a first order numerical scheme, named IFCP. IFCP numerical scheme is constructed by using a suitable decomposition of a Roe matrix of system (4) by means of a parabolic viscosity matrix (see (Degond et al. 1999)), that captures information of the intermediate fields. IFCP is a path-conservative scheme in the sense defined in (Parés 2006).

IFCP numerical scheme can be written as follows

$$w_i^{n+1} = w_i^n - \frac{\Delta t}{\Delta x}\big(D^+_{i-1/2} + D^-_{i+1/2}\big), \qquad (7)$$

being $D^\pm_{i+1/2} = D^\pm_{i+1/2}(w_i, w_{i+1}, b_i, b_{i+1})$ defined by

$$\begin{aligned} D^\pm_{i+1/2} = \ & \frac{1}{2}\big(F(w^n_{i+1}) - F(w^n_i) + \mathcal{B}_{i+1/2} - \mathcal{S}_{i+1/2} \\ & \pm Q_{i+1/2}(w^n_{i+1} - w^n_i - A^{-1}_{i+1/2}\mathcal{S}_{i+1/2}) \end{aligned} \qquad (8)$$

where $\mathcal{B}_{i+1/2} = B_{i+1/2}(w_{i+1} - w_i)$ being

$$B_{i+1/2} = \int_0^1 B(\Phi(s; W_i, W_{i+1}))\, ds; \qquad (9)$$

$\mathcal{S}_{i+1/2} = S_{i+1/2}(b_{i+1} - b_i)$, where

$$S_{i+1/2} = \int_0^1 S(\Phi(s; W_i, W_{i+1}))\, ds. \qquad (10)$$

$A_{i+1/2} = J_{i+1/2} + B_{i+1/2}$, being $J_{i+1/2}$ a Roe linearization of the Jacobian of the flux F in the usual sense:

$$J_{i+1/2} \cdot (w_{i+1} - w_i) = F(w_{i+1}) - F(w_i); \qquad (11)$$

and $Q_{i+1/2}$ is a viscosity matrix.

Remark 2.1 *Note that the numerical scheme depends on the choice of the family of path Φ. This scheme is a path-conservative numerical scheme in the sense introduced by Parés in (Parés 2006). In (Castro et al. 2008) and (Parés & Muñoz 2009) it has been proved that, in general, the numerical solutions provided by a path-conservative numerical scheme converge to functions which solve a perturbed system in which an error source-term appears on the right-hand side. The appearance of this source term, which is a measure supported on the discontinuities, has been first observed in (Hou & LeFloch 1994) when a scalar conservation law is discretized by means of a nonconservative numerical method. Nevertheless, in certain special situations the convergence error vanishes for finite difference methods: this is the case for systems of balance laws (see (Muñoz & Parés 2011)). Moreover for more general problems, even when the convergence error is present, it may be only noticeable for very fine meshes, for discontinuities of large amplitude, and/or for large-time simulations: see (Castro et al. 2008), (Parés & Muñoz 2009) for details.*

The key point is the definition of the matrix $Q_{i+1/2}$, that in the case of the IFCP is defined by:

$$Q_{i+1/2} = \alpha_0 Id + \alpha_1 A_{i+1/2} + \alpha_2 A^2_{i+1/2}, \qquad (12)$$

where α_j, $j = 0, 1, 2$ are defined by:

$$\begin{aligned} \alpha_0 &= \delta_1\, \lambda_{4,i+1/2}\, \chi_{int} + \delta_{4,i+1/2}\, \lambda_{1,i+1/2} \chi_{int} \\ &\quad + \delta_{int}\, \lambda_{1,i+1/2}\, \lambda_{4,i+1/2}, \\ \alpha_1 &= -\lambda_1(\delta_4 + \delta_{int}) - \lambda_{4,i+1/2}(\delta_1 + \delta_{int}) \\ &\quad - \chi_{int}(\delta_{1,i+1/2} + \delta_{4,i+1/2}), \\ \alpha_2 &= \delta_1 + \delta_4 + \delta_{int}, \end{aligned} \qquad (13)$$

being

$$\begin{aligned} \delta_1 &= \frac{|\lambda_{1,i+1/2}|}{(\lambda_{1,i+1/2} - \lambda_{4,i+1/2})(\lambda_{1,i+1/2} - \chi_{int})}, \\ \delta_4 &= \frac{|\lambda_{4,i+1/2}|}{(\lambda_{4,i+1/2} - \lambda_{1,i+1/2})(\lambda_{4,i+1/2} - \chi_{int})}, \\ \delta_{int} &= \frac{|\chi_{int}|}{(\chi_{int} - \lambda_{1,i+1/2})(\chi_{int} - \lambda_{4,i+1/2})}, \end{aligned}$$

where $\lambda_{1,i+1/2} < \lambda_{2,i+1/2} < \lambda_{3,i+1/2} < \lambda_{4,i+1/2}$ are the eigenvalues of matrix $A_{i+1/2}$ and

$$\chi_{int} = \mathcal{S}_{ext} \max(|\lambda_{2,i+1/2}|, |\lambda_{3,i+1/2}|), \qquad (14)$$

with

$$\mathcal{S}_{ext} = \begin{cases} \text{sgn}(\chi_{ext}), & \text{if } (\chi_{ext}) \neq 0, \\ 1, & \text{otherwise}, \end{cases} \qquad (15)$$

where $\chi_{ext} = \lambda_{1,i+1/2} + \lambda_{4+i+1/2}$.

It can be proved that IFCP scheme is linearly L^∞ stable under the usual CFL condition

$$\max\left\{\left|\lambda_{l,i+1/2}\right|, 1 \le l \le 4,\ i \in \mathbb{Z}\right\} \frac{\Delta t}{\Delta x} = CFL \le 1. \qquad (16)$$

Remark 2.2 *Note that the coefficients α_i are defined in terms of the eigenvalues of the matrix $A_{i+1/2}$. Here, we use the first order approximations defined in (Schijf & Schonfeld 1953) to estimate the wave speeds $\lambda_{l,i+1/2}$, $l = 1, \cdots, 4$.*

Remark 2.3 *Note that if $\alpha_0 = (1-\omega)\frac{\Delta x}{\Delta t}$, $\alpha_1 = 0$ and $\alpha_2 = \omega\frac{\Delta t}{\Delta x}$, then the numerical scheme (7)-(8) coincides with the family introduced in (Castro et al. 2010). This family contains, as particular cases, a well-balanced extension of the Lax-Friedrichs ($\omega = 0$), Lax-Wendroff ($\omega = 1$), FORCE ($\omega = \frac{1}{2}$), and GFORCE ($\omega = \frac{1}{1+CFL}$) methods.*

Remark 2.4 *Notice that in the definition of (8) the term*

$$C = Q_{i+1/2} A^{-1}_{i+1/2} \mathcal{S}_{i+1/2},$$

that can be interpreted as the upwinding part of the source term discretization, makes no sense if one of the eigenvalues of $A_{i+1/2}$ vanishes. In this case the problem is said to be resonant. Resonant problems exhibit an additional difficulty, as weak solutions may not be uniquely determined by their initial data, and the limits of the numerical solutions may depend both on the family of paths and the numerical scheme itself. The analysis of this difficulty is beyond the scope of this work. Here, we follow the strategy described in (Fernández et al. 2011) to get rid of this difficulty and to obtain well-balanced numerical schemes for a given set of stationary solutions.

2.1 Extension to high order

In order to define a high order numerical scheme for system (4), we follow the procedure described in (Castro et al. 2006). First, a high order reconstruction operator of the form $P^t_W(x) = (P^t_w(x), P_b(x))^T$ is considered, that is, an operator that associates, to a given sequence $\{W_i(t) = (w_i(t), b_i)^T\}$, two new sequences $\left\{W^-_{i+1/2}(t) = (w^-_{i+1/2}(t), b^-_{i+1/2})^T\right\}$, $\left\{W^+_{i+1/2}(t) = (w^+_{i+1/2}(t), b^+_{i+1/2})^T\right\}$ in such a way that, whenever

$$w_i(t) = \frac{1}{\Delta x}\int_{I_i} w(x,t)\,dx$$

$$b_i = \frac{1}{\Delta x}\int_{I_i} b(x)\,dx$$

for some regular function $W = (w, b)^T$, then

$$(w^\pm_{i+1/2}, b^\pm_{i+1/2}) = (w(x_{i+1/2}, t), b(x_{i+1/2}))^T + O(\Delta x^p),$$

$$\forall i \in \mathbb{Z}.$$

Here, we propose the following semi-discrete high order numerical scheme for (4) (see (Castro et al. 2006)):

$$\begin{aligned} w_i'(t) = \; & -\frac{1}{\Delta x}\left(D^+_{i-1/2} + D^-_{i+1/2}\right) \\ & -\frac{1}{\Delta x}\left(F(w^-_{i+1/2}(t)) - F(w^+_{i-1/2}(t))\right) \\ & -\frac{1}{\Delta x}\int_{I_i} B(P^t_{w_i}(x))(P^t_{w_i}(x))_x\,dx \\ & +\frac{1}{\Delta x}\int_{I_i} S(P^t_{w_i}(x))(P_{b_i}(x))_x\,dx, \end{aligned} \tag{17}$$

with $D^\pm_{i+1/2} = D(w^-_{i+1/2}(t), w^+_{i+1/2}(t), b^-_{i+1/2}, b^+_{i+1/2})$ and where $w^\pm_{i+1/2}(t)$ and $b^\pm_{i+1/2}$ are the reconstructed values at $x_{i+1/2}$ of $w(x,t)$ and $b(x)$, respectively. $P^t_{w_i}(x)$ and $P_{b_i}(x)$ are functions defined in I_i such that

$$\begin{aligned} \lim_{x\to x^+_{i-1/2}} (P^t_{w_i}(x), P_{b_i}(x)) &= (w^+_{i-1/2}(t), b^+_{i-1/2}), \\ \lim_{x\to x^-_{i+1/2}} (P^t_{w_i}(x), P_{b_i}(x)) &= (w^-_{i+1/2}(t), b^-_{i+1/2}). \end{aligned} \tag{18}$$

Fourth order Romberg quadrature formula is used to compute the integrals

$$\int_{I_i} B(P^t_{w_i}(x))(P^t_{w_i}(x))_x \text{ and } \int_{I_i} S(P^t_{w_i}(x))(P_{b_i}(x))_x.$$

Remark 2.5 *Note that high order schemes for conservative systems only depend on $w^\pm_{i+1/2}$, where they depend on $P^t_{w_i}$ and P_{b_i} for nonconservative systems (see (Castro et al. 2006)).*

Finally, a high order TVD-Runge-Kutta discretization can be used for the time-stepping (see (Gottlieb & Shu 1998)). Concerning the high order reconstruction operator, we usually use the PHM (piecewise hyperbolic method) introduced in (Marquina 1994). The extension to 2D systems is straightforward following (Castro et al. 2009) and (Gallardo et al. 2011).

3 NUMERICAL TESTS

In this section we present some numerical tests. In the first one, a battery of numerical tests is presented to study the dependency of the sediment layer profile and the generated tsunami with respect to the friction angle δ_0 and the ratio of densities, r. In the second one, the generation and propagation of tsunami on a real bathymetry is considered. In both cases, a GPU implementation of the previous scheme in two-dimensional domains has been used. Modern Graphics Processing Units (GPUs) offer hundreds of processing units optimized for massively performing floating point operations in parallel and have shown to be a cost-effective way to obtain a substantially higher performance in the applications related to shallow water flows due to the high exploitable parallelism which

exhibits the finite volume schemes (see for example: (Castro et al. 2011),(Brodtkorb et al. 2011) or (Gallardo et al. 2011)). Here, a MPI-CUDA implementation like the one presented in (**?**) has been performed to increase the speed-up of the computations up to two-orders of magnitude using a cluster of NVIDIA GTX-490 graphics cards with respect to a mono-core implementation in a modern CPU (Intel Xeon E5430 (2.66 GHz 12MB L2 Cache)).

3.1 Test 1

A battery of numerical tests is presented here to study numerically the dependency of the sediment layer profile and the generated tsunami with respect to the friction angle δ_0 and the ratio of densities, r. The effective angle of repose of the sediment layer after an avalanche is also measured at the stationary state. Let us consider a square domain of 10 m side, centered at the origin, with a flat bottom topography, that is, $b = -2$. As initial condition, we set $\boldsymbol{u}_1 = \boldsymbol{u}_2 = \mathbf{0}$ and

$$h_2(x, y, 0) = \begin{cases} 1, & \text{if } \|(x, y)\| < 1, \\ 0, & \text{otherwise,} \end{cases}$$

$h_1(x, y, 0) = 2 - h_2(x, y, 0)$. Free boundary conditions are imposed at both channels ends. The CFL parameter is set to 0.8.

Table 1: Effective angle of repose ($r = 0.4$, $\delta_0 = 20^o$)

Δx	max	mean	Δx	max	mean
0.1	18.03^o	8.43^o	0.05	19.16^o	8.46^o
0.02	19.69^o	8.46^o			

In Figure 1 we compare the final stationary interface that we obtain for three different meshes with $\Delta x = \Delta y \in \{0.1, 0.05, 0.02\}$ for $r = 0.4$ and $\delta_0 = 20^o$. Only some small differences near the "wet/dry" fronts can be observed. Table 1 shows the maximum and the mean effective angle of repose of the sediment layer after the landslide at the stationary state. As expected, the maximum value is under $\delta_0 = 20^o$, while the mean value is close to 8.5^o.

Figure 2 shows the profiles of the sediment layer at the stationary state for $r = 0.4$, $\Delta x = \Delta y = 0.05$ and $\delta_0 \in \{10^o, 15^o, 20^o, 25^o, 30^o\}$ and Table 2 shows the maximum and mean effective angle of repose of the sediment layer after the landslide. As expected, the maximum value is always under δ_0. Figure 3 shows the maximum of the free surface, $\eta = h_1 + h_2 - 2.0$, vs. δ_0. Figure 3 gives an idea of the amplitude of the generated tsunami. Note that the amplitude decreases for bigger values of the parameter δ_0.

Now, the parameter δ_0 is set to 20^o and $r \in \{0.0, 0.1, 0.2, 0.3, 0.4\}$. Figure 4 shows the profiles of the sediment layer at the stationary state for $\Delta x = \Delta y = 0.05$ and Table 3 shows the maximum and mean effective angle of repose of the sediment layer after the landslide. Again, the maximum value is always under δ_0. Note that the maximum value decreases with r while the mean increases with respect to r. Nevertheless, the variations are not relevant. More differences can be observed in the stationary profile of the second layer (see Figure 4), in particular the position of the front decreases with r, as well as the maximum height of the sediment layer. Figure 5 shows the maximum of the free surface, $\eta = h_1 + h_2 - 2.0$, vs. r. As expected, the amplitudes of the generated tsunami are bigger for smaller values of r.

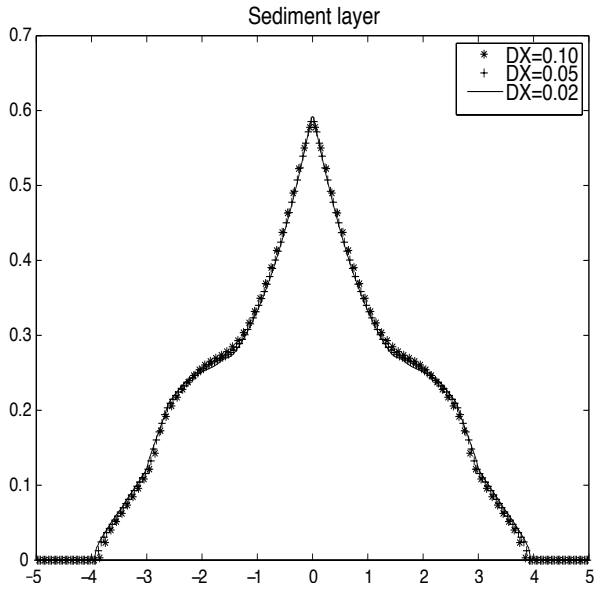

Figure 1: Sediment layer at stationary state $\Delta x = \Delta y \in \{0.1, 0.05, 0.02\}$, ($\delta_0 = 20^o$, $r = 0.4$).

Table 2: Effective angle of repose ($r = 0.4$)

δ_0	max	mean	δ_0	max	mean
10^o	9.82^o	2.84^o	15^o	14.51^o	5.35^o
20^o	19.16^o	8.46^o	25^o	23.90^o	12.05^o
30^o	29.42^o	16.13^o			

Table 3: Effective angle of repose ($\delta_0 = 20^o$)

r	max	mean	r	max	mean
0.0	19.64^o	8.07^o	0.1	19.56^o	8.22^o
0.2	19.37^o	8.30^o	0.3	19.23^o	8.41^o
0.4	19.16^o	8.46^o			

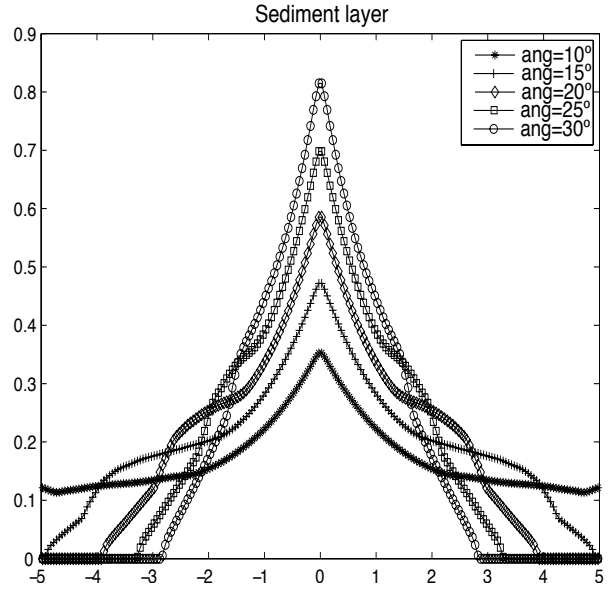

Figure 2: Sediment layer depth at the stationary state for $r = 0.4$ and $\delta_0 \in \{10^o, 15^o, 20^o, 25^o, 30^o\}$.

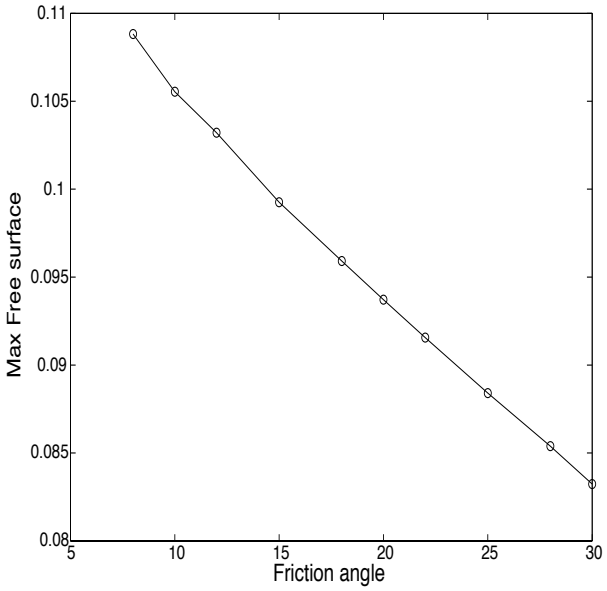

Figure 3: Maximal height of the free surface for $r = 0.4$ and $\delta_0 \in \{10^o, 15^o, 20^o, 25^o, 30^o\}$.

3.2 A tsunami generated by submarine landslide over real bathymetry

There are geological evidences about a tsunami generated by a submarine landslide located in the continental margin of Alboran island (western Mediterranean). The initial landslide area is located at southwest of Alboran island and covers an area about 9.5 km^2 where water depth range varies from 100 to 1000 m. Deposit covers an area of about 30 km^2. In this section we show an advanced numerical experiment that consist on starting from the current bathymetry, reconstruct the pre-tsunami paleo-bathymetry and then, simulate the landslide and the generated tsunami.

A rectangular 180 km $\times$ 190 km with $\Delta x = \Delta y = 25$ m grid has been considered (54720000 cells). The simulated time covers 3600 s after the tsunami is triggered. We set, CFL $= 0.9$, $r = 0.55$, $c_i = 10^{-5}$, and $\delta_0 = 10^\circ$.

Figures 6 and 7 show the current bathymetry and the reconstructed pre-tsunami original bathymetry.

Figures 8 and 9 show two different stages of the propagated tsunami. It can be observed how the shape of the tsunami varies according to the bathymetry; while the bathymetry is smoother southwards from the Alborani canyon, the shape of the tsunami wave is almost symmetric, while northwards, the sharper bathymetry effects are quite more visible.

Finally in Figure 10 it is shown a wave height time series extracted from a point near to Málaga (located in the north-west of the domain). We can observe that the tsunami wave arrives to this point about 32 mins after the tsunami is triggered. The first wave height is very small, just about 7-8 cm, then, two minutes later, a larger negative wave (about -40 cm height) arrives followed, 4 minutes later, by a larger wave of about 50 cm height. After this wave, other waves appear with lower height. We can remark than due to the geometry of the Málaga bay, some of these waves are reflected producing resonant effects.

4 CONCLUSIONS

In this work, a high order extension of the IFCP scheme has been introduced to solve a two-layer Savage-Hutter type model to simulate tsunamis generated by landslides. IFCP is a method constructed by a suitable decomposition of a Roe matrix $A_{i+1/2}$, whose viscosity matrix is computed by a linear combination of the identity matrix, $A_{i+1/2}$ and $A^2_{i+1/2}$ and whose coefficients are given in terms of the eigenvalues of $A_{i+1/2}$. The resulting numerical scheme is linearly L_∞-stable and well-balanced for the water at rest solution. A GPU implementation has been performed to speed up the computations. Two numerical tests have been presented: in the first one, a study the dependency of the sediment layer profile and the generated tsunami with respect to the friction angle δ_0 and the ratio of densities, r has been performed. In the second one, the generation and propagation of tsunami in the Alboran See using a real bathymetry have been performed.

Acknowledgements: This research has been partially supported by the Spanish Government Research projects MTM2009-11923. The numerical computations have been performed at the Laboratory of Numerical Methods of the University of Málaga.

REFERENCES

Asunción, M. de la & Mantas, J.M. & Castro, M.J. & Fernández, E.D. (2011). An MPI-CUDA

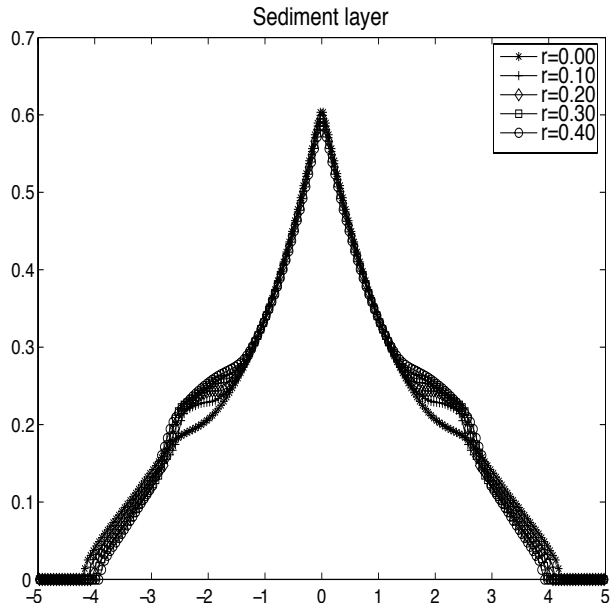

Figure 4: Sediment layer depth at the stationary state for $\delta_0 = 20^o$ and $r \in \{0, 0.1, 0.2, 0.3, 0.4\}$

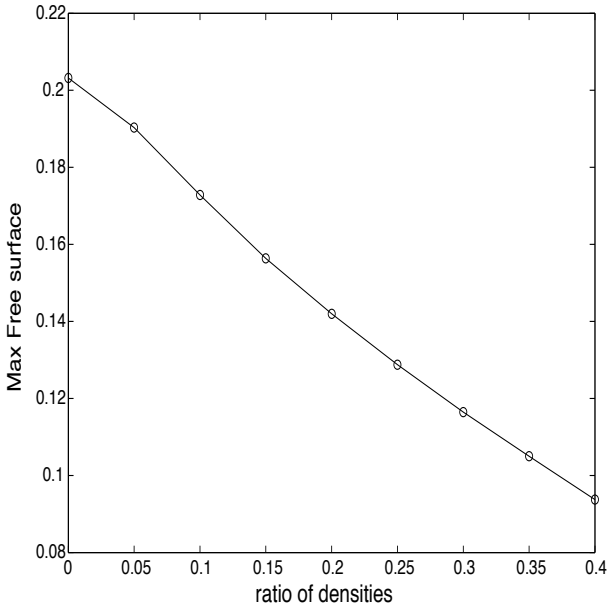

Figure 5: Maximal height of the free surface for $\delta_0 = 20^o$ and $r \in \{0, 0.1, 0.2, 0.3, 0.4\}$.

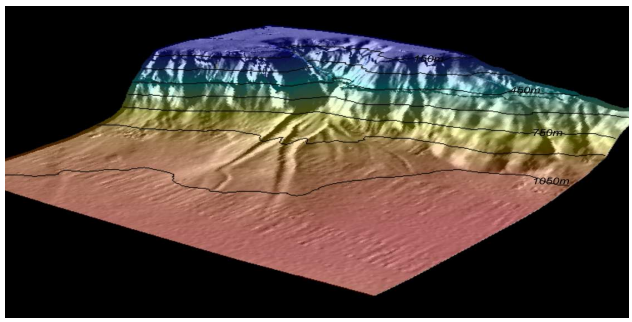

Figure 6: Current bathymetry

implementation of an improved Roe method for two-layer shallow water systems. *J. Parallel and Distributed Computing* (In Press, DOI:10.1016/j.jpdc.2011.07.012).

Brodtkorb, A. & Hagen, T. & Lie,K.A. & Natvig, J. (2011). Simulation and visualization of the saint-venant system using GPUs. *Computing and Visualization in Science*, 1–13.

Castro, M.J. & Gallardo, J.M. & Parés, C. (2006). High order finite volume schemes based on reconstruction of states for solving hyperbolic systems with nonconservative products. Applications to shallow-water systems. *Math. Comp*. 75:1103–1134.

Castro, M.J. & LeFloch, P.G. & Muñoz, M.L. & Parés, C. 2008. Why many theories of shock waves are necessary: Convergence error in formally path-consistent schemes. *J. Comp. Phys.* 3227:8107–8129.

Castro, M.J. & Fernández, E.D. & Ferreiro, A.M. & García, J.A. & Parés, C. 2009. High order extensions of Roe schemes for two dimensional nonconservative hyperbolic systems. *J. Sci. Comp.* 39:67–114.

Castro, M.J. & Pardo, A. & Parés, C. & Toro, E.F. 2010. On some fast well-balanced first order solvers for nonconservative systems. *Math. Comp.* 79:1427–1472.

Castro, M.J. & Ortega, S. & Asunción, M. de la & Mantas, J.M. & Gallardo, J.M. 2011. GPU computing for shallow water flow simulation based on finite volume schemes. *Comptes Rendus Mécanique* 339(2-3):165–184, High Performance Computing.

Dal Maso, G. & LeFloch, P.G. & Murat, F. 1995. Definition and weak stability of nonconservative products. *J. Math. Pures Appl.* 74:483–548.

Degond, P. & Peyrard, P.F. & Russo, G. & Villedieu, Ph. 1999. Polynomial upwind schemes for hyperbolic systems. *C. R. Acad. Sci. Paris* 328:479–483.

Fernández, E.D. & Bouchut, F. & Bresh, D. & Castro, M.J. & Mangeney, A. 2008. A new Savage-Hutter type model for submarine avalanches and generated tsunami. *J. Comp. Phys.* 227:7720–7754.

Fernández, E.D. & Castro, M.J. & Parés, C. 2011. On an Intermediate Field Capturing Riemann Solver Based on a Parabolic Viscosity Matrix for the Two-Layer Shallow Water System. *J. Sci. Comput.* 48(1-3):117–140.

Gallardo, J.M. & Ortega, S. & Asunción, M. de la & Mantas, J.M. 2011. Two-dimensional com-

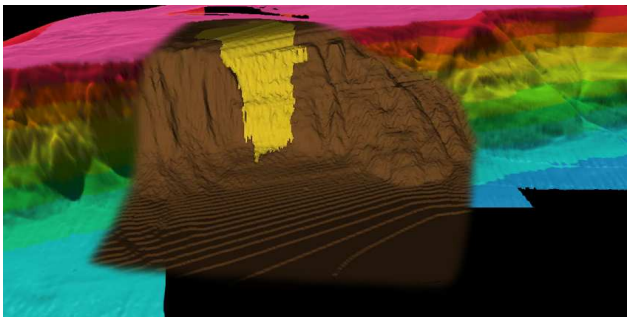

Figure 7: Supposed paleo-bathymetry before the landslide

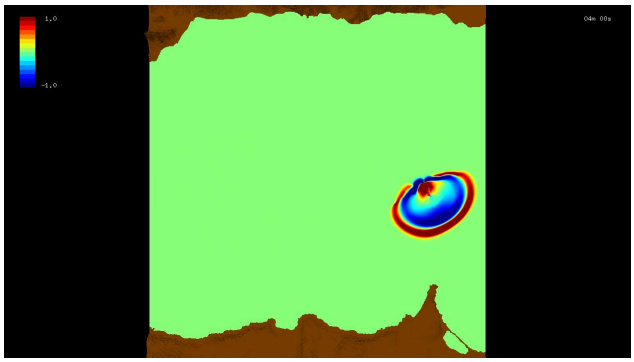

Figure 8: Free surface height at t=4.00 min

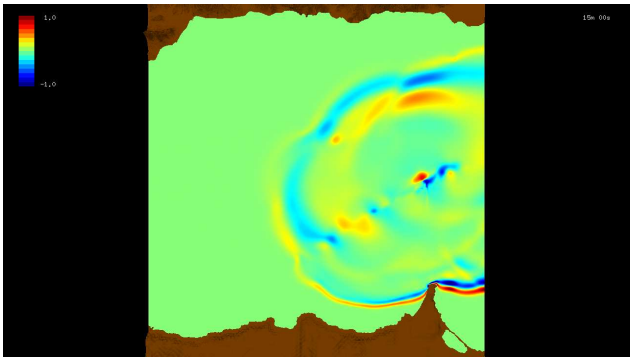

Figure 9: Free surface height at t=15.00 min

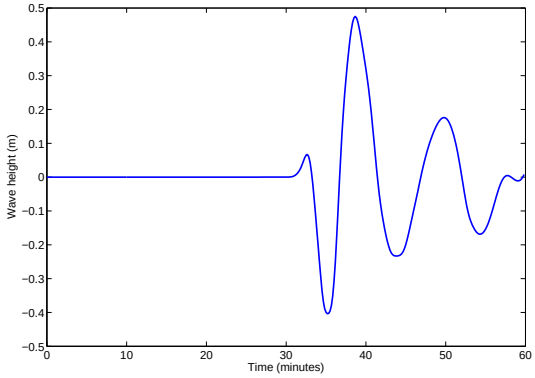

Figure 10: Wave height in a point near to Málaga (Iberian coast).

pact third-order polynomial reconstructions. Solving nonconservative hyperbolic systems using GPUs.*J. Sci. Comput.* 48(1-3):141–163.

Gottlieb, S. & Shu, C.W. 1998. Total variation diminishing Runge-Kutta schemes. *Math. Comp.* 67:73–85.

Hou, T.Y. & LeFloch, P.G. 1994. Why nonconservative schemes converge to wrong solutions: error analysis. *Math. of Comput.* 62:497–530.

Marquina, A. 1994. Local piecewise hyperbolic reconstructions for nonlinear scalar conservation laws. *SIAM J. Sci. Comp* 15:892–915.

Parés, C. & Castro, M.J. 2004. On the well-balance property of Roe's method for nonconservative hyperbolic systems. Applications to Shallow-Water Systems. *M2AN* 38(5):821–852.

Parés, C. 2006. Numerical methods for nonconservative hyperbolic systems: a theoretical framework. *SIAM J. Num. Anal.* 44(1):300–321.

Muñoz, M.L. & Parés, C. 2011. On the convergence and well-balanced property of path-conservative numerical schemes for systems of balance laws. *J. Sci. Comp.* 48(1-3):274–295.

Parés, C. & Muñoz Ruíz, M.L. 2009. On some difficulties of the numerical approximation of nonconservative hyperbolic systems. *Boletín SEMA* 47:23–52.

Schijf, J.B. & Schonfeld, J.C. 1953. Theoretical considerations on the motion of salt and fresh water. *In Proc. of the Minn. Int. Hydraulics Conv.*, 321–333. Joint meeting IAHR and Hyd. Div. ASCE.

Toumi, I. 1992. A weak formulation of Roe approximate Riemann solver. *J. Comp. Phys.* 102(2):360–373.